Small-scale behavior of Hall magnetohydrodynamic turbulence

Julia E. Stawarz[*]

Department of Astrophysical and Planetary Sciences, University of Colorado, Boulder, Colorado 80309, USA
and Laboratory for Atmospheric and Space Physics, University of Colorado, Boulder, Colorado 80303, USA

Annick Pouquet

Laboratory for Atmospheric and Space Physics, University of Colorado, Boulder, Colorado 80303, USA

Decaying Hall magnetohydrodynamic (HMHD) turbulence is studied using three-dimensional (3D) direct numerical simulations with grids up to 768^3 points and two different types of initial conditions. Results are compared to analogous magnetohydrodynamic (MHD) runs and both Laplacian and Laplacian-squared dissipative operators are examined. At scales below the ion inertial length, the ratio of magnetic to kinetic energy as a function of wave number transitions to a magnetically dominated state. The transition in behavior is associated with the advection term in the momentum equation becoming subdominant to dissipation. Examination of autocorrelation functions reveals that, while current and vorticity structures are similarly sized in MHD, HMHD current structures are narrower and vorticity structures are wider. The electric field autocorrelation function is significantly narrower in HMHD than in MHD and is similar to the HMHD current autocorrelation function at small separations. HMHD current structures are found to be significantly more intense than in MHD and appear to have an enhanced association with strong alignment between the current and magnetic field, which may be important in collisionless plasmas where field-aligned currents can be unstable. When hyperdiffusivity is used, a longer region consistent with a $k^{-7/3}$ scaling is present for right-polarized fluctuations when compared to Laplacian dissipation runs.

PACS number(s): 52.30.Cv, 94.05.Lk, 52.35.Ra, 47.27.ek

I. INTRODUCTION

Turbulence is a ubiquitous phenomenon that is believed to play a role in the dynamics of a variety of space plasma environments, including the solar corona [1,2], solar wind [3–5], planetary magnetospheres [6–11], and the interstellar medium [12,13]. While viscosity and resistivity are often invoked to model the dissipation in simulations of magnetohydrodynamic (MHD) turbulence, the collisionless nature of many space plasmas means a more complete description of the kinetic scales, where the fluid approximation breaks down, is needed to understand the small scales of plasma turbulence. Understanding how kinetic processes interact with a turbulent environment is currently an active area of research [14] and from a numerical standpoint is made difficult by the computational challenges associated with both obtaining the large-scale separations inherent to turbulent flows and accurately describing the kinetic scales of the plasma.

Nonlinearities associated with turbulence are thought to be important down into the kinetic scales [15–17]. Kinetic effects can result in observed changes to the slope of the energy spectrum and ultimately contribute to the dissipation of energy from the turbulence [18–24]. A number of kinetic scale features observed in the solar wind and magnetosphere are thought to be associated with turbulence. It has been suggested that observations of electron phase-space holes and double layers in the Earth's plasma sheet are caused by currents generated by turbulence [11,25,26]. The behavior of Langmuir waves observed in the solar wind has been attributed to turbulence [27]. Osman *et al.* [28] found an association

between kinetic scale instabilities and the turbulent energy cascade rate. New missions, such as the recently launched Magnetospheric Multiscale mission [29], with small spatial separations between multiple spacecraft, will help enhance the understanding of kinetic scale turbulence and make necessary approaches using fully kinetic physics or a more complete generalized Ohm's law, such as Hall magnetohydrodynamics (HMHD).

One way to begin looking at kinetic effects in a turbulent environment numerically is to consider more accurate approximations to the kinetic equations, such as the HMHD equations. While not a complete model of the kinetic scales, HMHD begins to incorporate kinetic effects by allowing for the decoupling of ion and electron motions at scales below the ion inertial length through the addition of the Hall term in Ohm's Law. The Hall effect has been studied extensively in the context of magnetic reconnection using Harris sheet configurations and HMHD is found to be the minimum plasma model necessary to obtain fast reconnection rates comparable to those obtained from more complete kinetic plasma simulations [30–32]. Signatures of the Hall term have been found in the Earth's magnetosphere [33,34] and in laboratory plasmas [35]. Under some parameter regimes in the solar wind, a steepening of the spectral slope from either a Kolmogorov spectrum [36] or the so-called Iroshnikov-Kraichnan spectrum [37] has been associated with the ion inertial length [38]. So-called plasmoids, as observed in the magnetotail by the Cluster spacecrafts, are viewed as the signature of multiple reconnection events in the Hall regime and are linked to substorms [39].

Spectra of HMHD turbulence are expected to be steeper than MHD at scales below the ion inertial length in both the strong and weak turbulence regimes, with a power-law

---

[*]julia.stawarz@colorado.edu

slope of $-7/3$ for the magnetic field in strong turbulence [40]. Steepening of the solar wind spectra above the ion cyclotron frequency has been attributed to HMHD effects [41–43]. Some numerical simulations have reported power-law slopes similar to $-7/3$ [44–46]; however, it is difficult to determine the spectral slope for HMHD at the numerical resolutions available today. Meyrand and Galtier [47] found that right and left circularly polarized fluctuations have different power-law slopes with right polarizations showing a $-7/3$ slope and left polarizations showing a $-11/3$ slope and showed heuristically that the magnetic field should follow these power laws.

Previous studies of HMHD turbulence have found that although MHD scales control some important average properties of the system, such as the energy decay rate [48], the structures present in the flow can be significantly altered. Miura and Hori [46] and Miura and Araki [49] examined the current and vorticity structures and found that there are smaller scale structures present in HMHD; they speculated the much lower amplitude vorticity structures were excited by the enhanced small-scale magnetic field activity in HMHD. Larger-scale vorticity structures were found to be potentially more tubular than in MHD, although roll-up of vorticity sheets as well as current sheets have also been observed in MHD turbulence [50]. Two-dimensional (2D) simulations have found reconnection sites in the turbulence become similar in structure to laminar studies of HMHD reconnection which exhibit bifurcated current sheets and quadrupolar magnetic fields [51]. Dmitruk and Matthaeus [52] found that while the magnetic field was largely unchanged by the addition of the Hall effect, the electric field was more intermittent. Using theoretical calculations and low-resolution simulations, Mininni *et al.* [53] found that the Hall effect alters the coupling between the magnetic field and velocity and can result in a backscattering of energy which is not seen in MHD. Reduced HMHD models, which describe the system in the presence of a strong background magnetic field, have also been examined and it was found that in this context structures widen and generate internal eddies and currents resulting in an apparent reduction in intermittency [54–56].

In this paper, we use three-dimensional (3D) direct numerical simulations (DNS) to examine the behavior of HMHD turbulence in the absence of forcing. The features in both Fourier and real space are examined to better understand the small-scale behavior. In Sec. II the HMHD equations and initial conditions used in the DNS are discussed. Section III A presents the numerical results in Fourier space and provides an interpretation for the behavior. Section III B discusses the numerical results in real space. Section III C briefly presents runs using hyperdiffusivities and compares the results to the traditional diffusivity runs presented in Secs. III A and III B. Section IV summarizes the results and discusses some possible implications for collisionless plasmas.

II. EQUATIONS

The incompressible HMHD equations in dimensionless form are given by

$$\frac{\partial \mathbf{b}}{\partial t} = \nabla \times (\mathbf{v} \times \mathbf{b}) - \epsilon_H \nabla \times (\mathbf{j} \times \mathbf{b}) + \eta \nabla^2 \mathbf{b} - \eta' \nabla^4 \mathbf{b}, \quad (1)$$

$$\frac{\partial \mathbf{v}}{\partial t} = -\mathbf{v} \cdot \nabla \mathbf{v} - \nabla P + \mathbf{j} \times \mathbf{b} + \nu \nabla^2 \mathbf{v} - \nu' \nabla^4 \mathbf{v}, \quad (2)$$

$$\nabla \cdot \mathbf{v} = 0, \quad \nabla \cdot \mathbf{b} = 0, \quad (3)$$

where the velocity $\mathbf{v}$ and magnetic field $\mathbf{b}$ are in units of a characteristic velocity U_0 with the magnetic field expressed in Alfvén units, P is the particle pressure, and $\mathbf{j} = \nabla \times \mathbf{b}$ is the current density. The dissipation coefficients ν and η are the traditional kinematic viscosity and magnetic diffusivity respectively, whereas ν' and η' are hyperviscosity and hyperdiffusivity coefficients respectively associated with Laplacian-squared dissipative terms. In this paper $\nu = \eta$, $\nu' = \eta'$, and only one form of dissipative term is used in any given run (that is to say, if $\nu \neq 0$, then $\nu' = 0$ and vice versa). The mass density is taken to be uniform and is absorbed into the nondimensionalization of the pressure. With the addition of the Hall term, the dimensionless parameter $\epsilon_H = d_i/L_0$ giving the ratio of the ion inertial length to the characteristic length scale of the system enters into the equations. If $\epsilon_H = 0$, then the HMHD equations reduce to the MHD equations. The electric field in HMHD is given by

$$\mathbf{e} = -\mathbf{v} \times \mathbf{b} + \epsilon_H \mathbf{j} \times \mathbf{b} + \eta \mathbf{j} - \eta' \nabla^2 \mathbf{j}. \quad (4)$$

Since multiple nonlinear terms are present in the HMHD system, three distinct "dissipation" scales can be defined by comparing the time scales associated with the nonlinear terms to the dissipation time scale. Using dimensional analysis, the conditions for these scales can be written as

$$\frac{1}{\nu}\sqrt{\frac{E_V(k_A)}{k_A}} = 1, \quad \frac{E_M(k_L)}{\nu\sqrt{k_L E_V(k_L)}} = 1,$$

$$\frac{\epsilon_H \sqrt{k_H E_M(k_H)}}{\eta} = 1, \quad (5)$$

for traditional viscosity and diffusivity and as

$$\frac{1}{\nu'}\sqrt{\frac{E_V(k_A)}{k_A^5}} = 1, \quad \frac{E_M(k_L)}{\nu'\sqrt{k_L^5 E_V(k_L)}} = 1,$$

$$\frac{\epsilon_H}{\eta'}\sqrt{\frac{E_M(k_H)}{k_H^3}} = 1, \quad (6)$$

for hyperviscosity and hyperdiffusivity. $E_V(k)$ and $E_M(k)$ are the kinetic and magnetic energy spectra respectively, k_A is the dissipation wave number associated with the advection term $(\mathbf{v} \cdot \nabla \mathbf{v})$, k_L is the dissipation wave number associated with the Lorentz force $(\mathbf{j} \times \mathbf{b})$, and k_H is the dissipation wave number associated with the Hall term $(\epsilon_H \nabla \times [\mathbf{j} \times \mathbf{b}])$. For $\nu = \eta$ or $\nu' = \eta'$, k_A is identical to the dissipation wave number for $\nabla \times (\mathbf{v} \times \mathbf{b})$. In MHD, where the Hall term is absent and there is generally near equipartition between magnetic and kinetic energy in the small scales [57], all of the dissipation scales coincide. The largest of the wave numbers k_A, k_L, and k_H corresponds to the overall dissipation scale of the system where all nonlinearities are subdominant to dissipation. In this study, the numerical spectra output by the DNS are used in computing the dissipation wave numbers so as not to require assumptions for the spectral slopes that develop.

The HMHD equations can alternatively be written in the form [58]

$$\frac{\partial \mathbf{b}}{\partial t} = \nabla \times [(\mathbf{v} - \epsilon_H \mathbf{j}) \times \mathbf{b}] + \eta \nabla^2 \mathbf{b} - \eta' \nabla^4 \mathbf{b}, \quad (7)$$

$$\frac{\partial}{\partial t}(\mathbf{b} + \epsilon_H \boldsymbol{\omega}) = \nabla \times [\mathbf{v} \times (\mathbf{b} + \epsilon_H \boldsymbol{\omega})] + \nabla^2[\eta \mathbf{b} + \epsilon_H \nu \boldsymbol{\omega}]$$
$$- \nabla^4[\eta' \mathbf{b} + \epsilon_H \nu' \boldsymbol{\omega}], \quad (8)$$

with $\boldsymbol{\omega} = \nabla \times \mathbf{v}$ the vorticity. In the ideal system (neglecting dissipative terms), the fields $\boldsymbol{\Omega}_R \equiv \mathbf{b}$ and $\boldsymbol{\Omega}_L \equiv \mathbf{b} + \epsilon_H \boldsymbol{\omega}$ are frozen into the fields $\mathbf{u}_R \equiv \mathbf{v} - \epsilon_H \mathbf{j}$ and $\mathbf{u}_L \equiv \mathbf{v}$ respectively. That is to say, they obey the flux-conservation equations

$$\partial_t \boldsymbol{\Omega}_R = \nabla \times [\mathbf{u}_R \times \boldsymbol{\Omega}_R], \quad \partial_t \boldsymbol{\Omega}_L = \nabla \times [\mathbf{u}_L \times \boldsymbol{\Omega}_L]. \quad (9)$$

The fields $\mathbf{u}_{R,L}$ are equivalent to the HMHD version of the Elsässer variables in the limit $\epsilon_H k \gg 1$ [40].

The ideal invariants for the MHD system are the total energy (E_T), magnetic helicity (H_M), and cross helicity (H_C) defined as

$$E_T = E_V + E_M = \tfrac{1}{2}\langle |\mathbf{v}|^2 + |\mathbf{b}|^2 \rangle,$$
$$H_M = \tfrac{1}{2}\langle \mathbf{a} \cdot \mathbf{b} \rangle, \quad H_C = \tfrac{1}{2}\langle \mathbf{v} \cdot \mathbf{b} \rangle, \quad (10)$$

with $\langle ... \rangle$ denoting a volume average and where $\mathbf{b} = \nabla \times \mathbf{a}$, $\mathbf{a}$ being the magnetic potential. In HMHD, H_C is no longer conserved and instead the generalized helicity defined as

$$H_G = \tfrac{1}{2}\langle (\mathbf{a} + \epsilon_H \mathbf{v}) \cdot (\mathbf{b} + \epsilon_H \boldsymbol{\omega}) \rangle = H_M + 2\epsilon_H H_C + \epsilon_H^2 H_V \quad (11)$$

is conserved [59]. $H_V = \langle \mathbf{v} \cdot \boldsymbol{\omega} \rangle / 2$ is the kinetic helicity, which is an invariant in ideal hydrodynamics. Relative helicities are defined as

$$\sigma_M = \frac{\mathbf{a} \cdot \mathbf{b}}{|\mathbf{a}||\mathbf{b}|}, \quad \sigma_C = \frac{\mathbf{v} \cdot \mathbf{b}}{|\mathbf{v}||\mathbf{b}|},$$
$$\sigma_G = \frac{(\mathbf{a} + \epsilon_H \mathbf{v}) \cdot (\mathbf{b} + \epsilon_H \boldsymbol{\omega})}{|\mathbf{a} + \epsilon_H \mathbf{v}||\mathbf{b} + \epsilon_H \boldsymbol{\omega}|}, \quad \sigma_V = \frac{\mathbf{v} \cdot \boldsymbol{\omega}}{|\mathbf{v}||\boldsymbol{\omega}|} \quad (12)$$

and measure the degree of alignment (cosine of angle) between the vectors in the conserved helicities. Additional alignments considered in this study are

$$\sigma_R = \frac{\mathbf{u}_R \cdot \boldsymbol{\Omega}_R}{|\mathbf{u}_R||\boldsymbol{\Omega}_R|}, \quad \sigma_L = \frac{\mathbf{u}_L \cdot \boldsymbol{\Omega}_L}{|\mathbf{u}_L||\boldsymbol{\Omega}_L|}, \quad \sigma_{jb} = \frac{\mathbf{j} \cdot \mathbf{b}}{|\mathbf{j}||\mathbf{b}|}. \quad (13)$$

These alignments inform us on the strength of the nonlinear terms appearing in the primitive equations. In Fourier space these alignments are defined using cross-spectra. The magnetic polarization, which measures the direction of circular polarization relative to the magnetic field, is given by $P_M = \sigma_M \sigma_C$ computed in Fourier space. $P_M > 0$ and $P_M < 0$ correspond to left and right circularly polarized fluctuations respectively [47].

For $\nu = \eta$, the average energy dissipation in the system for both MHD and HMHD is given by $\nu \Omega_T$, where $\Omega_T = \langle |\mathbf{j}|^2 \rangle + \langle |\boldsymbol{\omega}|^2 \rangle$ is the total enstrophy. For decaying turbulence, the time at which Ω_T is maximum corresponds to when the turbulence is most fully developed. In the hyperdiffusive case, when $\nu' = \eta'$, the average energy dissipation in the system is given by $\nu' \mathcal{P}_T$, where $\mathcal{P}_T = \langle |\nabla^2 \mathbf{b}|^2 \rangle + \langle |\nabla^2 \mathbf{v}|^2 \rangle$ is the total palinstrophy.

The linearized incompressible HMHD equations support two types of wave modes; the right circularly polarized whistler wave and the left circularly polarized ion cyclotron wave [60]. For the whistler and ion cyclotron modes $P_M = -1$ and $P_M = 1$, respectively. At small wave numbers the two modes merge onto the same dispersion relation consistent with MHD where circular polarization is not a relevant parameter and there is only one wave mode, the Alfvén wave. The linear ratio of magnetic to kinetic energy is given by

$$\frac{E_M(k)}{E_V(k)} = \frac{k^2 \epsilon_H^2}{4} \left(\pm 1 + \sqrt{1 + \frac{4}{k^2 \epsilon_H^2}} \right)^2 \quad (14)$$

with k the wave number and $+$ or $-$ giving the right- and left-polarized modes respectively. In the limit of $k\epsilon_H \gg 1$, the whistler mode is magnetically dominated with $E_M(k)/E_V(k) = k^2 \epsilon_H^2$ and the ion cyclotron mode is kinetically dominated with $E_M(k)/E_V(k) = (k^2 \epsilon_H^2)^{-1}$.

An alternative way to "linearize" the system is if the fluctuations have perfect alignment between u_R and Ω_R and between u_L and Ω_L, which makes all nonlinear terms zero [42,58]. This type of configuration is referred to as a double curl Beltrami solution and gives equivalent solutions to the small-amplitude linear fields but for arbitrary amplitude fluctuations. The necessary alignments would need to occur as a result of the nonlinear dynamics and it is not obvious the alignment should occur in any arbitrary turbulent system.

A. Initial conditions

All runs are performed using the Geophysical High-Order Suite for Turbulence (GHOST) code [61]. GHOST is a general-purpose pseudospectral community code with periodic boundary conditions and parallelized up to in excess of $\approx 130\,000$ processors using a hybrid (MPI-OpenMP) methodology, which is advantageous at high resolutions.

Two types of initial conditions are examined in this study, one using a prescribed set of phase relationships and the other one using randomly phased fluctuations. Details about the runs are listed in Table I. The first set of initial conditions is a modification of the Orszag-Tang vortex based on Biskamp and Welter [62] and extended to 3D in a manner similar to Politano *et al.* [63]:

$$\mathbf{b}_{OT} = b_0[\sin(y + 4.1) + \sin(z), -2\sin(2x + 2.3) + \sin(z), \sin(x) + \sin(y)], \quad (15)$$

$$\mathbf{v}_{OT} = v_0[\sin(y + 0.5), -\sin(x + 1.4), 0]. \quad (16)$$

The values of b_0 and v_0 are set such that $\langle |\mathbf{b}_{OT}|^2 \rangle = 0.64$ and $\langle |\mathbf{v}_{OT}|^2 \rangle = 1.36$ initially, resulting in nearly equal values of $\langle |\mathbf{j}|^2 \rangle$ and $\langle |\boldsymbol{\omega}|^2 \rangle$. Runs are performed at resolutions using 256^3, 512^3, and 768^3 grid points in a cubic box and with periodic boundary conditions. At all resolutions $\epsilon_H = 0.0$ or 0.2. Additionally at 256^3, runs with $\epsilon_H = 0.1$ and 0.5 are performed. At 768^3, the initial condition for the $\epsilon_H = 0.2$ run is taken to be the peak of dissipation from the 768^3 $\epsilon_H = 0.0$ run. This method of starting an HMHD run from the peak of dissipation was tested at 256^3 resolution and produced comparable results to a 256^3 HMHD run started from scratch

TABLE I. Resolution, value of ν (which is the same as the value of η), value of ϵ_H, and eddy turn-over time $\tau_{\rm nl}$ at the peak of Ω_T (or $\mathcal{P}_T$ for the hyperdiffusive runs) for the 16 runs performed in this study. In the Run ID, OT stands for the Orszag-Tang initial condition, R stands for the random initial condition, M stands for MHD, H stands for HMHD, the number after H gives $10\epsilon_H$, and K4 indicates the use of hyperdiffusivity. Run OTH2c is started from the OTMc peak of Ω_T.

Run ID	Resolution	ν or ν'	ϵ_H	$\tau_{\rm nl}$
OTMa,b,c	$256^3, 512^3, 768^3$	$1 \times 10^{-2}, 5 \times 10^{-3}, 3.3 \times 10^{-3}$	0.0	5.77, 4.39, 4.01
OTH1	256^3	1×10^{-2}	0.1	5.88
OTH2a,b	$256^3, 512^3$	$1 \times 10^{-2}, 5 \times 10^{-3}$	0.2	6.07, 5.11
OTH2c	768^3	3.3×10^{-3}	0.2	4.11
OTH5	256^3	1×10^{-2}	0.5	6.26
RMa,b,c	$128^3, 256^3, 512^3$	$2 \times 10^{-2}, 1 \times 10^{-2}, 5 \times 10^{-3}$	0.0	3.61, 3.43, 3.16
RH2a,b,c	$128^3, 256^3, 512^3$	$2 \times 10^{-2}, 1 \times 10^{-2}, 5 \times 10^{-3}$	0.2	3.26, 3.07, 2.84
RH2K4a,b	256^3	$2.5 \times 10^{-5}, 7 \times 10^{-6}$	0.2	2.53, 2.30

using the Orszag-Tang initial conditions. The initial relative helicities for all Orszag-Tang runs are $\sigma_M \sim \sigma_C \sim -0.2$ and $\sigma_V \sim 0.0$. Furthermore, at $\epsilon_H = 0.2$, $\sigma_G \sim -0.28$, whereas for both $\epsilon_H = 0.1$ and 0.5, $\sigma_G \sim -0.26$ initially. Runs using this initial condition are denoted with an OT in Table I.

The second set of initial conditions initialize the fields $\mathbf{u}_L$ and $\mathbf{u}_R$ with random phases and power spectra which follow the form $E_{L,R}(k) = C_{L,R} k^4 \exp(-k^2/k_0^2)$. The wave number k_0 is set such that the spectra peak at $k = 2$ and C_L and C_R are set such that $\langle|\mathbf{u}_L|^2\rangle = 1.00$ and $\langle|\mathbf{u}_R|^2\rangle = 0.5$. Noting that $\epsilon_H^2 \langle|\mathbf{j}|^2\rangle = \langle|\mathbf{u}_R|^2\rangle + \langle|\mathbf{u}_L|^2\rangle - 2\langle\mathbf{u}_R \cdot \mathbf{u}_L\rangle$, the correlation between $\mathbf{u}_L$ and $\mathbf{u}_R$ is set such that the initial $\langle|\mathbf{j}|^2\rangle$ and $\langle|\boldsymbol{\omega}|^2\rangle$ are nearly equal. In the case of MHD, identical initial conditions to the HMHD case are used even though $\epsilon_H = 0$ in MHD. Random runs are performed at resolutions 128^3, 256^3, and 512^3 with $\epsilon_H = 0.0$ and 0.2 in all cases. Initially $\sigma_M \sim 0.24$, $\sigma_C \sim 0.01$, $\sigma_V \sim -0.04$, and $\sigma_G \sim 0.17$. Two HMHD runs with this initial condition have also been performed using hyperdiffusivity for comparison with the regular diffusivity results. This initial condition is denoted with an RM or RH (for MHD and HMHD respectively) in Table I.

Physically, the OT configuration is structured with an X point centered on a stagnation point (with a sinusoidal variation in the third direction) so current sheets are known to form rather rapidly. In the formulation of the OT configuration presented here, phase shifts are introduced that break some of the symmetry present in the traditional configuration. On the other hand, random initial conditions are possibly more representative of a natural flow, with less symmetries and thus possibly more complicated to analyze in terms of structures in physical space. Both types of initial conditions are studied here to cover a larger dynamical range. The relative helicity coefficients are chosen to represent generic data; indeed, if zero or 1, they represent very specific and unlikely configurations unless one imposes the symmetries (such as in the case of the Taylor Green or Beltrami configurations). Moreover, when taking the relative helicities close to unity, the nonlinear terms are strongly damped and the evolution out of that state will be slow [64].

The eddy turn-over time is defined as $\tau_{\rm nl} \equiv L_{\rm int}/\langle|\mathbf{v}|^2\rangle^{1/2}$, where $L_{\rm int}$ is the integral scale defined as

$$L_{\rm int} = 2\pi \frac{\int [E_V(k)/k]dk}{\int E_V(k)dk}. \tag{17}$$

Table I also gives the value of $\tau_{\rm nl}$ for each run computed at the peak of Ω_T or $\mathcal{P}_T$.

III. NUMERICAL RESULTS

Figure 1 plots E_T and Ω_T as a function of time for runs RH2c and RMc. The following sections are focused on data taken from near the peak of Ω_T (for the two runs shown in Fig. 1 this corresponds to $t \sim 1.925$ for run RH2c and $t \sim 1.75$ for run RMc in simulation units) unless otherwise noted. Despite HMHD showing enhanced small-scale activity (see Fig. 2), HMHD tends to show slightly smaller Ω_T than MHD resulting in slightly different profiles of E_T. The smaller Ω_T is linked to the steepening of the HMHD spectrum at scales below the ion inertial length. The predicted spectral slope for magnetic fluctuations in HMHD is steeper than -2. In the DNS presented here the total energy spectrum also tends to become steeper than k^{-2} at near $1/\epsilon_H$ and since $\Omega_T(k) = k^2 E_T(k)$, the peak of the Ω_T spectrum will be near $1/\epsilon_H$. The steepening of the spectrum is not necessarily present in MHD until dissipation becomes significant and therefore a broader profile to the $\Omega_T(k)$ spectrum can be formed resulting in a larger average value of Ω_T when the spectrum is integrated. Even with smaller values of Ω_T on average, locally currents are enhanced significantly in HMHD (see Sec. III B). Figure 1 also shows the ratios of magnetic to kinetic energy and mean-square current to mean-square vorticity for the same runs. In both MHD and HMHD the flows tend to be magnetically dominated as interpreted from either ratio; for the random initial condition it is slightly less so in HMHD. The OT initial conditions and other resolutions (not displayed) behave similarly except for some slight differences in the ratios.

The behavior of the relative helicities as a function of time are similar between MHD and HMHD and therefore are not displayed. In all cases, σ_M shows the most growth over the course of the run. The value of σ_G also shows significant growth over the course of the HMHD runs likely associated with the presence of H_M in the definition of H_G.

A. Behavior in Fourier space

Figure 2 shows $E_T(k)$ for the runs analyzed in this study. The most distinct feature of the HMHD spectra is the excess of energy relative to MHD in the small scales in all cases, which is associated with the magnetic energy. The excess
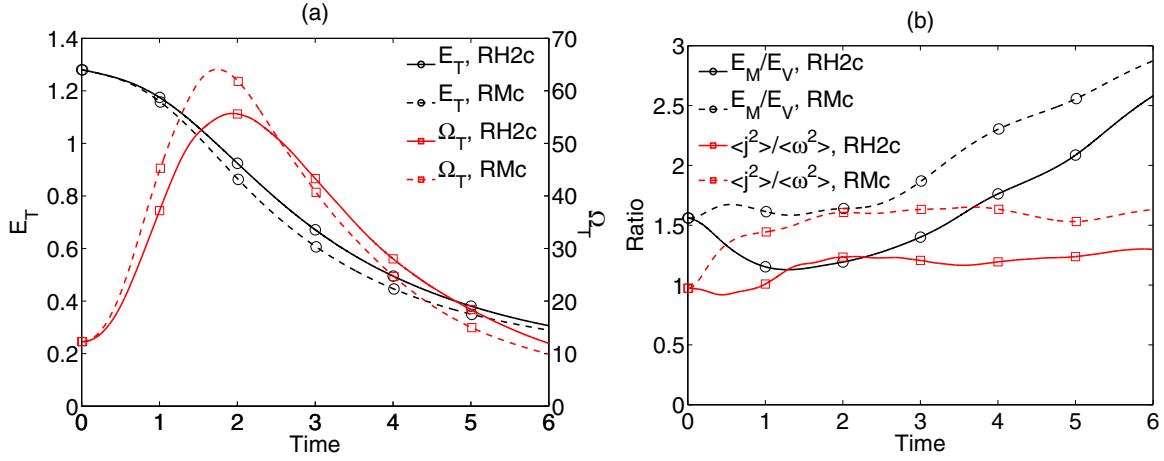
FIG. 1. (Color online) (a) Total energy (black circles) and enstrophy (red squares) as a function of time for RMc (dashed lines) and RH2c (solid lines). (b) Ratio of magnetic to kinetic energy and ratio of mean-square current to mean-square vorticity as a function of time for the same runs and in the same format as in panel (a).
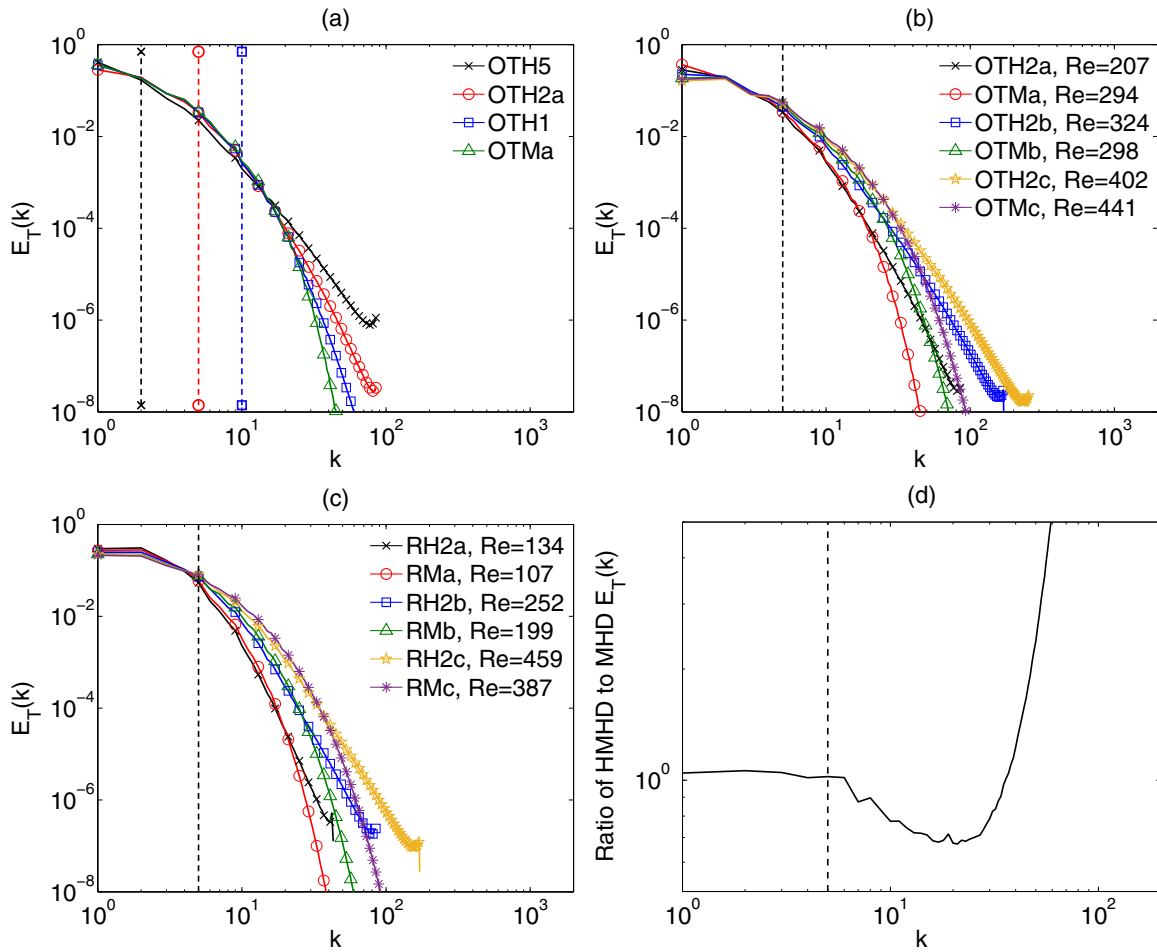

FIG. 2. (Color online) (a) $E_T(k)$ for runs OTMa, OTH1, OTH2a, and OTH5, which have varying values of ϵ_H. Vertical dashed lines mark $1/\epsilon_H$ with colors and markers corresponding to the run. (b) $E_T(k)$ for runs OTMa,b,c and OTH2a,b,c, which have varying Reynolds numbers. (c) $E_T(k)$ for runs RMa,b,c and RH2a,b,c, which have varying Reynolds numbers. In panels (b) and (c), Reynolds numbers $\mathrm{Re} = \langle |\mathbf{v}|^2 \rangle L_{\mathrm{int}}/\nu$ at the peak of Ω_T are given in the legend. (d) Ratio of $E_T(k)$ for run RH2c to $E_T(k)$ for run RMc. The region of negative slope indicates where HMHD is steeper than MHD. In panels (b)–(d) vertical dashed lines show $1/\epsilon_H$.

of energy becomes more pronounced as ϵ_H is increased [Fig. 2(a)]. While the spectra are similar for small wave numbers, at moderate wave number above $1/\epsilon_H$, the HMHD spectra tend to be slightly steeper than MHD consistent with theory (however, the exact spectral slope cannot be determined at the resolutions here) [40]. For reference, in the case of run RH2c, the steeper region lasts from roughly $k \sim 6$ to $k \sim 20$ as shown in Fig. 2(d). However, dissipation in the MHD cases quickly causes the MHD spectra to become steeper than HMHD; indeed, we take the same viscosity for the MHD and HMHD runs, but due to the fact that in MHD the production of small scales is not as intense as for HMHD, the runs have a larger dissipation range. In runs OTH1 and OTH2a, the steeper region is likely not evident because of the location of the dissipation scale. Run OTH2c likely does not show a steeper region because the run was continued from the peak of dissipation of the MHD version and the small to moderate wave numbers did not change significantly in the time it takes to reach the new peak in Ω_T.

As suggested by Meyrand and Galtier [47], another way of examining the spectra in HMHD is to look at the energy spectra of strongly circularly polarized fluctuations. Figure 3

plots energy spectra constructed using only wave vectors with $P_M > 0.3$ and $P_M < -0.3$ or $P_M > 0.7$ and $P_M < -0.7$. In both the random and OT initial conditions the left-polarized spectra are steeper than the right-polarized spectra, as was found by Meyrand and Galtier [47] using hyperdiffusivities, indicating the excess energy at small scales seen in Fig. 2 is associated with right-polarized fluctuations. However, in the random case the left-polarized spectrum dominates in the large scales, whereas right and left polarizations are roughly in equipartition in the large scales of the OT runs. This behavior is likely related to the mean-square values of $\mathbf{u}_R$ and $\mathbf{u}_L$ which are roughly equal initially in the OT runs and set to be a factor of two apart initially in the random runs. Using a threshold of $|P_M| > 0.3$, short regions where the right and left spectra may be compatible with spectral slopes of $-7/3$ and $-11/3$ respectively can be found [Fig. 3(b)], consistent with the results of Meyrand and Galtier [47]. When the threshold is set to 0.7 [Fig. 3(c)], the $-7/3$ scaling extends over a wide range in the right-polarized spectrum in run RH2c, but the left-polarized spectrum is even steeper than $-11/3$. The break in the $-7/3$ spectrum for run RH2c in Fig. 3(c) at $k \sim 65$ roughly corresponds with the wave number k_H.
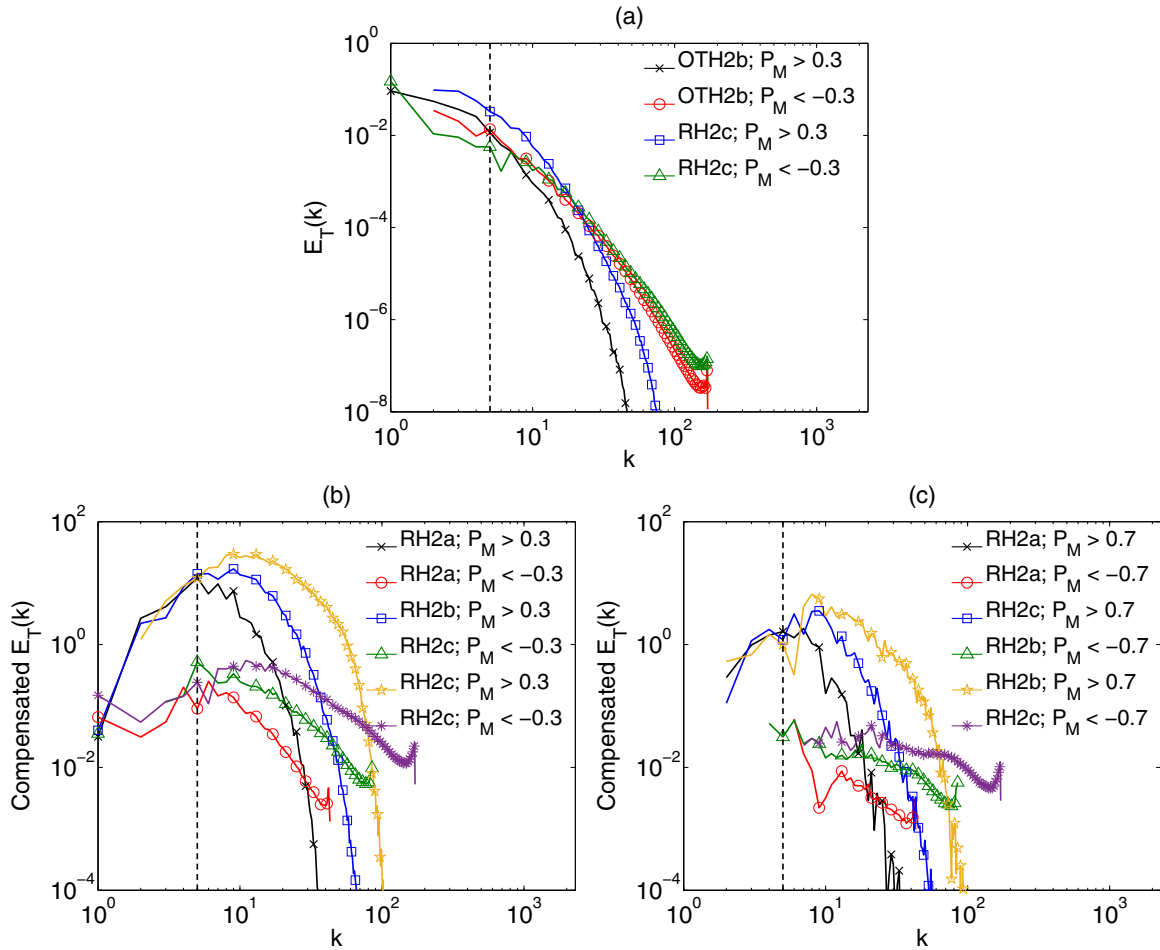

FIG. 3. (Color online) (a) Spectra for fluctuations with $|P_M| > 0.3$ for runs OTH2b and RH2c. (b) Spectra for the same values of P_M as panel (a) but compensated by either $k^{11/3}$ for positive P_M (left-polarized ion cyclotron fluctuations) or $k^{7/3}$ for negative P_M (right-polarized whistler fluctuations) as predicted and observed in hyperdiffusive simulations by Meyrand and Galtier [47]. (c) Spectra with $|P_M| > 0.7$ compensated by either $k^{11/3}$ for positive P_M or $k^{7/3}$ for negative P_M. The compensated spectra are for runs RH2a, RH2b, and RH2c, which have various Reynolds numbers. In all panels, vertical dashed lines mark $1/\epsilon_H$.
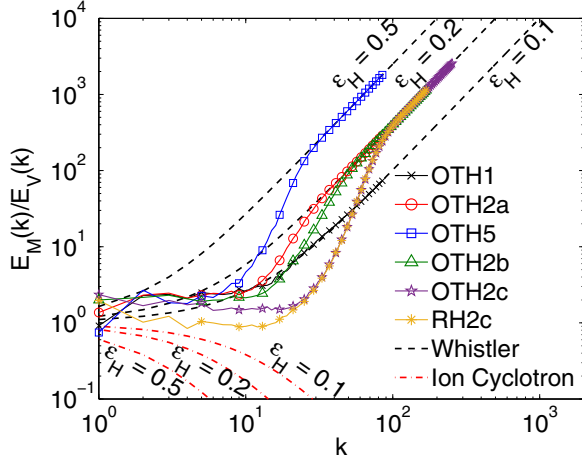
FIG. 4. (Color online) Ratio of magnetic to kinetic energy spectra near the peak of Ω_T for runs OTH1, OTH2a, OTH2b, OTH2c, OTH5, and RH2c. For all runs, the ratio at large wave numbers matches the linear prediction for whistler waves. At lower wave numbers the energy is roughly in equipartition, consistent with the behavior of MHD. The random HMHD runs tend to be more kinetically dominated than the OT runs or the random MHD runs at low wave numbers.

FIG. 5. (Color online) Spectra of the alignments associated with the double curl Beltrami state [58] for run RH2c. The solid black curve gives σ_R and the red dashed curve gives σ_L. An absolute value is taken before averaging over spherical shells to avoid cancellation of positive and negative alignment. The vertical dashed line marks $1/\epsilon_H$.

Figure 4 plots $E_M(k)/E_V(k)$ for a variety of HMHD runs. The spectra in MHD are found to be in near equipartition (within a factor of 2) at all scales (see, for example, Stawarz *et al.* [57]), and this is the case for all of the MHD runs performed in this study (not shown). In HMHD, the spectra are in near equipartition at large scales and then transition to a magnetically dominated state in the small scales, where the spectra exactly match the whistler wave linear prediction. In the context of a shell model for HMHD, Galtier and Buchlin [65] also noted that a magnetically dominated regime could be obtained under certain parameter regimes. The wave number at which the transition occurs is above $1/\epsilon_H$ in most cases and moves to larger wave number as the Reynolds number is increased. In the region of near equipartition, the random runs have relatively more kinetic energy than the OT runs, likely because $|\mathbf{u}_R| < |\mathbf{u}_L|$ and left-polarized fluctuations (expected to be kinetically dominated from linear theory) dominate the spectra in the large scales. Based on Fig. 3, it is not surprising the small scales are magnetically dominated since the left polarizations fall off more steeply than the right polarizations.

One possible explanation for the seemingly linear behavior observed in the small scales in Fig. 4 is through the presence of the double curl Beltrami configuration in the small scales. To examine the role of this configuration in the dynamics of HMHD turbulence, Fig. 5 plots σ_R and σ_L computed in Fourier space [see Eq. (13) for the real-space formulation] for run RH2c. Absolute values are performed before averaging over spherical shells in Fourier space to create the spectra to avoid cancellations of positive and negative alignment. All HMHD runs analyzed behave similarly to the displayed curves. If both σ_R and σ_L correspond to full alignment, then the nonlinear dynamics stop and in the presence of a uniform background magnetic field, B_0, the linear solution is
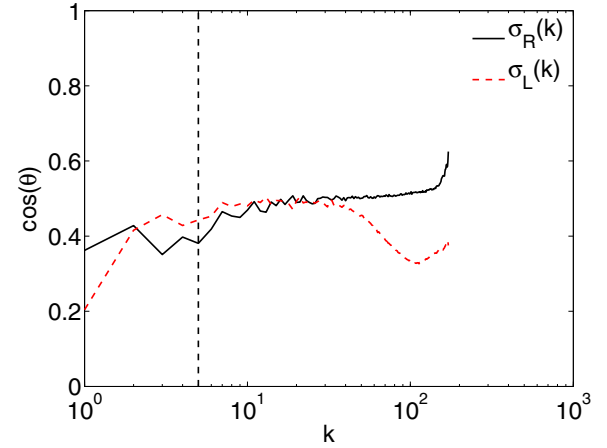
obtained. In the simulations presented here, no B_0 is explicitly imposed; however, it is possible for the largest scale magnetic fluctuations to appear as a quasiuniform field to the small-scale fluctuations, provided there is enough scale separation [37]. Starting at roughly $1/\epsilon_H$, σ_R and σ_L are constant at a value of roughly 1/2. At $k \sim 40$ for run RH2c, σ_L begins to decrease significantly and then increases somewhat at $k \sim 100$. The lack of both large σ_R and σ_L in the small scales seems to contradict the idea that the small scales are in a double curl Beltrami state. However, the effect may be obscured by the difficulty of separating B_0 from the fluctuations in the current simulations. The theory of Krishan and Mahajan [42] only requires the nonlinear fluctuations, and not the background field, to have the double curl Beltrami alignments.

To better understand the change in behavior present in Fig. 4, consider the Fourier transform of the induction and vorticity equations [Eq. (1) and the curl of Eq. (2)] neglecting dissipation

$$\frac{\partial \mathbf{b}_k}{\partial t} = i\mathbf{k} \times ([\mathbf{v} \times \mathbf{b}]_k - \epsilon_H[\mathbf{j} \times \mathbf{b}]_k) \qquad (18)$$

$$\frac{\partial \boldsymbol{\omega}_k}{\partial t} = i\mathbf{k} \times ([\mathbf{v} \times \boldsymbol{\omega}]_k + [\mathbf{j} \times \mathbf{b}]_k), \qquad (19)$$

where $i = \sqrt{-1}$, $\mathbf{k}$ is the wave vector, and subscript k denotes the Fourier transform of a quantity ($[...]_k$ is the Fourier transform of a whole nonlinear term). From dimensional analysis, one might expect the Hall term to dominate the induction equation at scales below the ion inertial length ($\epsilon_H k \gg 1$), so at small scales the $[\mathbf{v} \times \mathbf{b}]_k$ term will be neglected and $\mathbf{v}$ no longer influences the evolution of $\mathbf{b}$. However, it is unclear from dimensional analysis alone which terms may be important in the vorticity equation. An important distinction between the MHD scales and HMHD scales is that in terms of powers of k the nonlinear terms in the induction equation scale as the momentum equation at MHD scales and the vorticity equation at HMHD scales.

Different behaviors of the vorticity and therefore the velocity fluctuations will occur depending on the relative importance of the $[\mathbf{v} \times \boldsymbol{\omega}]_k$ and $[\mathbf{j} \times \mathbf{b}]_k$ terms. If $\mathbf{k} \times [\mathbf{j} \times \mathbf{b}]_k$ dominates the vorticity equation, which could happen if $\mathbf{v}$ is significantly more aligned with $\boldsymbol{\omega}$ than $\mathbf{b}$ is with $\mathbf{j}$, if $|\mathbf{v}||\boldsymbol{\omega}| \ll |\mathbf{j}||\mathbf{b}|$, or if the angles between the nonlinear terms and $\mathbf{k}$ are significantly different, then the vorticity equation (with a factor of $-\epsilon_H$) will evolve identically to the induction equation. We can then write $-\epsilon_H \partial_t \boldsymbol{\omega}_k = \partial_t \mathbf{b}_k$, which, assuming small-scale fluctuations are initially zero, can be integrated to obtain $-\epsilon_H \boldsymbol{\omega}_k = \mathbf{b}_k$. Since each component of $\boldsymbol{\omega}_k$ and $\mathbf{b}_k$ are equal the magnitudes must be equal and, using the fact that $|\boldsymbol{\omega}_k| = k|\mathbf{v}_k|$, an expression for the ratio of magnetic to kinetic energy can be written

$$\frac{E_M(k)}{E_V(k)} = \epsilon_H^2 k^2. \tag{20}$$

This expression is true for both linear and nonlinear small-scale HMHD fluctuations where the $[\mathbf{j} \times \mathbf{b}]_k$ term dominates over the $[\mathbf{v} \times \boldsymbol{\omega}]_k$ term in the vorticity equation. Equation (20) can similarly be obtained from the magnetic vector potential and velocity equations if the pressure term is neglected. In the linear solution, obtaining the lower frequency and kinetic energy dominated ion cyclotron wave requires the influence of the $[\mathbf{v} \times \mathbf{b}]_k$ term, which has been neglected in obtaining Eq. (20). Equation (20) is equivalent to the linear prediction for whistler waves in the limit $\epsilon_H k \gg 1$, which is the region where the ratios in Fig. 4 match up with the linear prediction. Galtier and Buchlin [65] also found a relationship between magnetic and kinetic energy consistent with Eq. (20) for some parameters, as well as an alternative kinetically dominated regime in other parameter regimes based on shell-model results and it was noted through heuristic arguments involving the balance of nonlinear time scales that various behaviors of $E_M(k)/E_V(k)$ may be linked to the wide range of spectral slopes observed at subion scales in the solar wind. The DNS results presented in this study only show a transition to the magnetically dominated state.

To understand the state described by Eq. (20) in more physical terms, first note that $\mathbf{v}$ is a mass weighted average of ion and electron velocities and since ions have much more mass than electrons, $\mathbf{v}$ is approximately the ion fluid velocity. Also note that $\epsilon_H \mathbf{j}$ is the difference between ion and electron velocities. Therefore, the dominance of the Hall term in the induction equation corresponds to a state where ions are approximately stationary compared to electrons and only electron motions are carrying the currents in the small scales. With the Lorentz force dominating over advection in the vorticity equation, small-scale fluctuations in $\mathbf{v}$ are simply responding to the magnetic field fluctuations and in turn electron velocity fluctuations without any significant advection or feedback on the evolution of the magnetic field. This behavior is similar in some ways to the electron MHD approximation.

The relative importance of the various nonlinear terms in run RH2c is examined in Figs. 6(a) and 6(b), which show the ratios of the spectra associated with the nonlinear terms $[\mathbf{j} \times \mathbf{b}]_k$, $[\mathbf{v} \times \boldsymbol{\omega}]_k$, and $[\mathbf{v} \times \mathbf{b}]_k$ and their curls. In the magnetic vector potential equation, $\epsilon_H [\mathbf{j} \times \mathbf{b}]_k$ dominates over $[\mathbf{v} \times \mathbf{b}]_k$ at wave numbers larger than $1/\epsilon_H$. Since the derivative in time

of $\mathbf{a}$ is given by the electric field, this means that the Hall term is dominating the electric field at wave numbers above $1/\epsilon_H$. The actual wave number where the Hall term becomes dominant occurs at $k \sim 8$, which is consistent with the energy in the initial conditions mainly being located between $k = 1$ and $k = 2$, making L_0 slightly smaller than 2π. In the induction equation, $\epsilon_H \mathbf{k} \times [\mathbf{j} \times \mathbf{b}]_k$ is comparable to $\mathbf{k} \times [\mathbf{v} \times \mathbf{b}]_k$ at wave numbers above $1/\epsilon_H$ but does not become dominant until larger wave numbers. Based on the linear solution, left-polarized waves have equipartition between $\epsilon_H \mathbf{k} \times [\mathbf{j} \times \mathbf{b}]_k$ and $\mathbf{k} \times [\mathbf{v} \times \mathbf{b}]_k$ at wave numbers above $1/\epsilon_H$ [similarly to the midrange wave numbers in Fig. 6(b)], while in the right-polarized waves the Hall term dominates.

In the velocity equation, the term $[\mathbf{j} \times \mathbf{b}]_k$ is found to be comparable to $[\mathbf{v} \times \boldsymbol{\omega}]_k$ into the Hall regime, but in the small scales $[\mathbf{j} \times \mathbf{b}]_k$ is dominant. The wave number at which the ratio $[\mathbf{j} \times \mathbf{b}]_k^2/[\mathbf{v} \times \boldsymbol{\omega}]_k^2$ begins to increase roughly corresponds to the wave number where $E_M(k)/E_V(k)$ begins to increase towards the prediction of Eq. (20). In the vorticity equation, the ratio of $\mathbf{k} \times [\mathbf{j} \times \mathbf{b}]_k$ to $\mathbf{k} \times [\mathbf{v} \times \boldsymbol{\omega}]_k$ decreases with $\mathbf{k} \times [\mathbf{v} \times \boldsymbol{\omega}]_k$ dominating at wave numbers above $1/\epsilon_H$; however, the ratio begins to increase at moderate wave numbers and $\mathbf{k} \times [\mathbf{j} \times \mathbf{b}]_k$ dominates at the largest wave numbers. The change in behavior of the nonlinear terms in the vorticity equation seems to be associated with the change in behavior in the nonlinear terms of the velocity equation. The scale at which these changes in behavior occur appear to be associated with the scale k_A, which roughly is consistent with where $E_M(k)/E_V(k)$ begins to increase. The association with k_A is consistent with the transition to the magnetically dominated state occurring at larger wave number for higher Reynolds number as seen in Fig. 4. While $\mathbf{k} \times [\mathbf{j} \times \mathbf{b}]_k$ does not dominate the vorticity equation at the scale where the energy begins to become magnetically dominated, $\mathbf{k} \times [\mathbf{j} \times \mathbf{b}]_k$ does dominate the vorticity equation at the scales where $E_M(k)/E_V(k)$ follows Eq. (20) as expected. k_A is smaller than the overall dissipation wave number of the system (in this case k_H), indicating that the interplay of dissipation with the various nonlinear terms can lead to different regimes of HMHD turbulence. Similar results to run RH2c are found for the other HMHD runs. Figure 6(c) shows spectra of σ_{jb}, σ_V, and σ_C, which are the alignments associated with the nonlinear terms. The spectra of σ_{jb} and σ_V are similar at small scales indicating it is the magnitudes of the vectors that are causing $[\mathbf{j} \times \mathbf{b}]_k$ to dominate the velocity equation rather than the angles between the vectors.

Although in the example shown k_L seems to roughly correspond to a change in behavior in $[\mathbf{v} \times \mathbf{b}]_k^2/(\epsilon_H^2 [\mathbf{v} \times \boldsymbol{\omega}]_k^2)$ and in $|\mathbf{k} \times [\mathbf{j} \times \mathbf{b}]_k|^2/|\mathbf{k} \times [\mathbf{v} \times \boldsymbol{\omega}]_k|^2$, examination of other runs reveals that k_L is not associated with strong changes in behavior as is the case with k_A. In the runs at resolution 512^3, k_H seems to be associated with the Hall term dominating the induction equation; however, at lower resolutions this is not necessarily the case.

The decrease in σ_L in Fig. 5 may be associated with the increase in the importance of $\mathbf{v} \times \mathbf{b}$ compared to the $\epsilon_H \mathbf{v} \times \boldsymbol{\omega}$ term [Fig. 6(a)] and increase in σ_C to the value of σ_V [Fig. 6(c)]. Both of these quantities are relevant to σ_L and show significant changes in behavior at $k \sim 40$, which is where σ_L begins to decrease. σ_L begins to increase again when $\sigma_C \sim \sigma_V$.
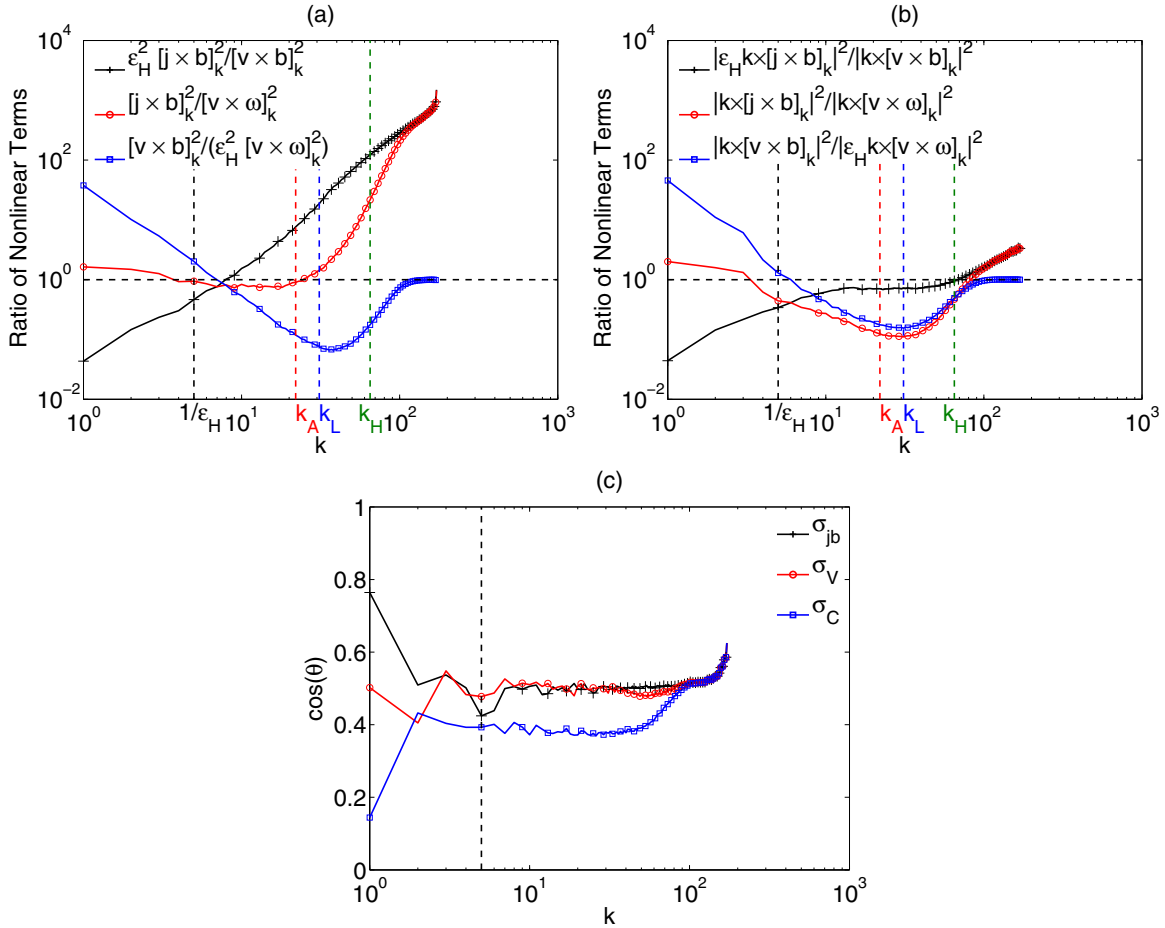
FIG. 6. (Color online) (a) Ratios of the spectra of the nonlinear terms present in the magnetic vector potential, velocity, and "uncurled" $\mathbf{\Omega}_L$ equations. The horizontal dashed line marks a value of unity, and the vertical dashed lines mark the ion inertial length ($1/\epsilon_H$) and dissipation scales given by Eq. (5) (k_A, k_L, and k_H). (b) Same as in panel (a) but for the nonlinear terms in the induction, vorticity, and $\mathbf{\Omega}_L$ equations. (c) Spectra of the cosine of the angles between the vectors involved in the nonlinear terms (σ_{jb}, σ_V, and σ_C). In creating the spectra, the absolute value of the correlation is taken before averaging over spherical shells to avoid cancellation of positive and negative alignment. The vertical dashed line gives the ion inertial length. All three plots are for run RH2c. Other HMHD runs show the same general behavior.

B. Behavior in real space

The occurrence of strong localized structures at small scales is a hallmark of turbulent flows, for incompressible fluids [66] (see Ref. [67] for the supersonic case), as well as in MHD [68,69], where it can lead to finite dissipation in the limit of small viscosity and resistivity [50]. Indeed, in real space, coherent structures in the current, associated with intermittency [70,71, and references therein], play an important role. In the context of resistive MHD and Hall MHD, velocity gradients and currents are responsible for local dissipation of energy [50,63,68] (see also Ref. [72]). In collisionless plasmas, the current structures in particular are thought to play a key role in dissipation [11,73–75]; directional discontinuities are observed as well, often attributed to the Hall regime although they are also present in MHD at sufficiently high Reynolds numbers [76,77].

Figure 7 shows 2D cuts for the current, vorticity, and σ_{jb} near the peak of Ω_T for run OTH2b. The 2D cuts are for a subset of the domain located around the current structure containing the maximum current. For the cut in σ_{jb}, alignments less than 0.9 are masked out to highlight the most aligned structures. In

Fig. 7, white curves mark the half-maximum current contours and the white + marks the location of the maximum current. It is found that for both types of initial conditions, strong currents tend to be associated with regions of highly aligned magnetic field and current ($\sigma_{jb} \approx \pm 1$). σ_R shows similar results to σ_{jb}; however, this is not unexpected since in the small scales the Hall term dominates, which should give $\sigma_R \sim -\sigma_{jb}$. We also observe that in the vicinity of regions of high alignment, σ_{jb} can vary in sign (corresponding to parallel or antiparallel configurations of the fields), as was already observed in MHD for the velocity-magnetic field correlation [78].

To further examine this association, Fig. 8 plots probability distributions (PDFs) for various alignments conditioned on the strength of the current being greater than 75% of the maximum for runs OTH2b and RH2c. Since only a limited number of current structures form within the domain for the runs presented in this study, it is possible to obtain false peaks near strong alignment in the conditional PDFs if the current structures randomly coincide with regions of strong alignment. However, if the current structures are not fundamentally associated with a given alignment, the shape of the conditional PDF can significantly change in time as current
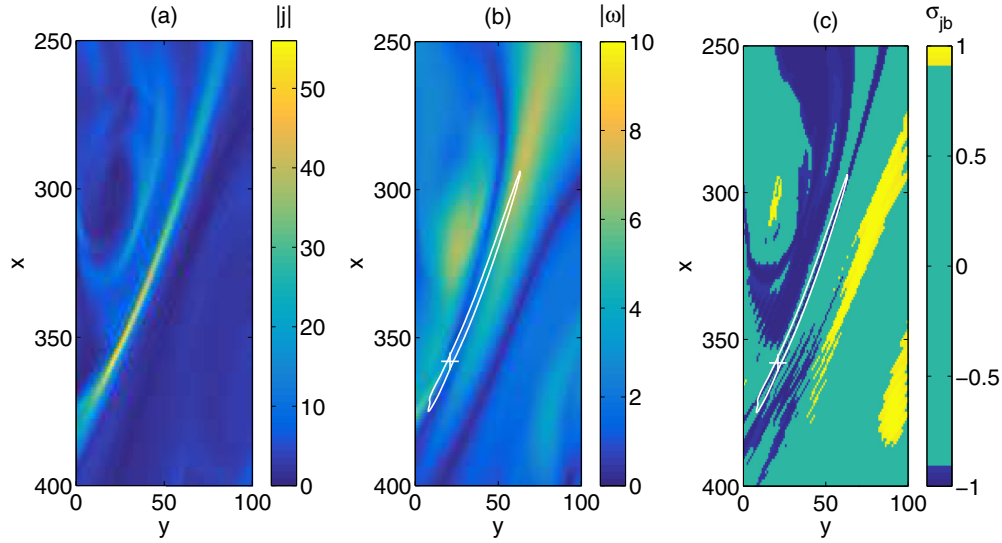
FIG. 7. (Color online) 2D cuts of $|\mathbf{j}|$ (a), $|\boldsymbol{\omega}|$ (b), and σ_{jb} (c) at the location of maximum current near the peak of Ω_T for run OTH2b. White crosses mark the location of maximum current and white curves give the half-maximum contours of the current. Values of $|\sigma_{jb}| < 0.9$ are masked out to highlight the highly aligned structures. The x and y axes are in units of grid points.
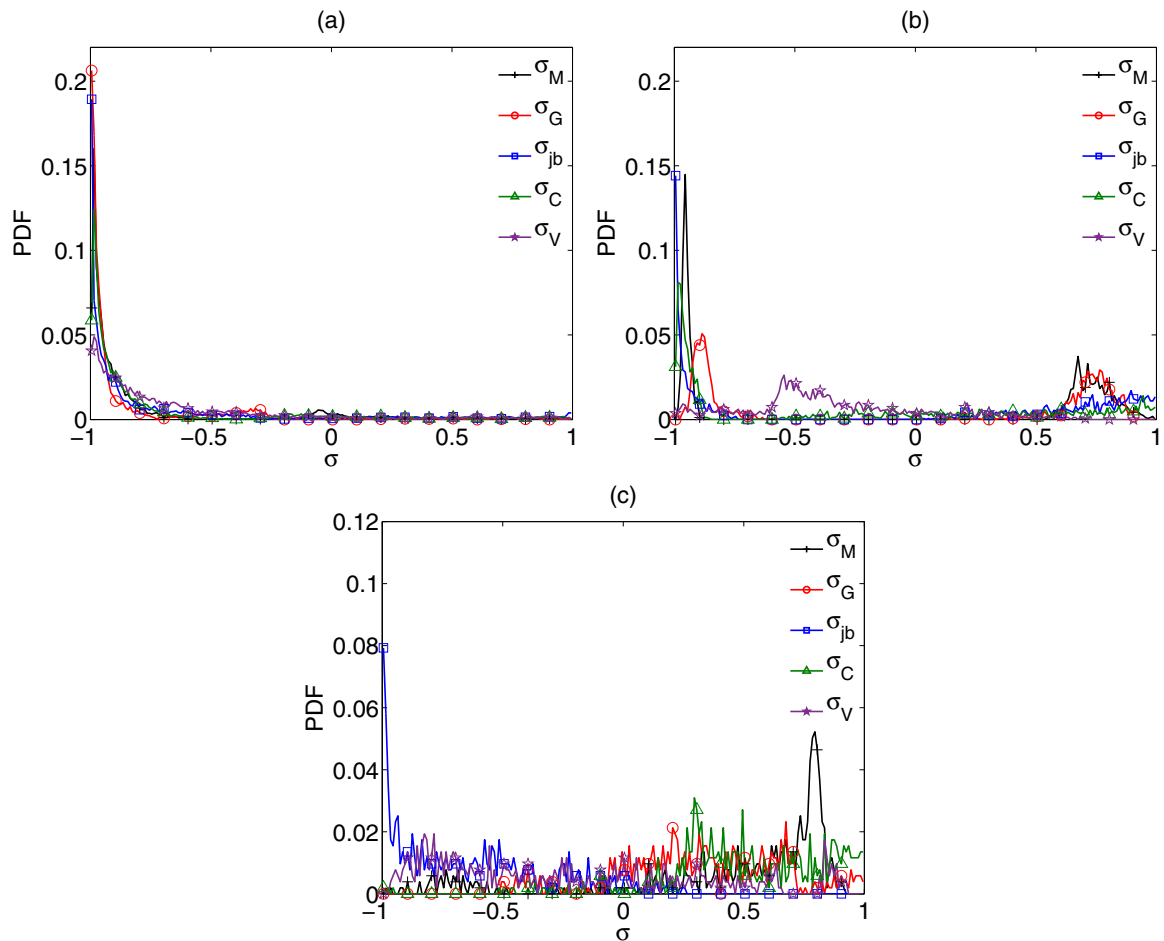

FIG. 8. (Color online) Conditional PDFs of σ_M, σ_G, σ_{jb}, σ_C, and σ_V for points where $|\mathbf{j}|$ is greater than 75% of the maximum. Panels (a) and (b) show run OTH2b at the time of peak Ω_T and 1.2 times the time of peak Ω_T respectively. Panel (c) shows run RH2c at the time of peak Ω_T. At all times and initial conditions examined, peaks in the conditional PDF for σ_{jb} are present at either $+1$ or at -1 (as plotted here).
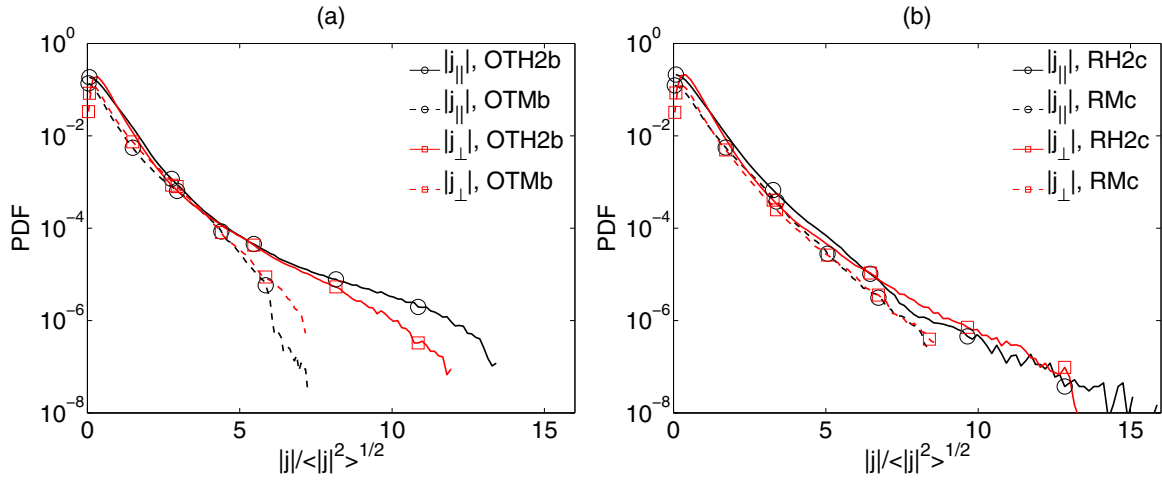
FIG. 9. (Color online) (a) Distributions of $|j_\parallel| = |\mathbf{j} \cdot \mathbf{b}|/|\mathbf{b}|$ (black circles) and $|j_\perp| = \sqrt{|\mathbf{j}|^2 - |j_\parallel|^2}$ (red squares) for runs OTH2b (solid lines) and OTMb (dashed lines). (b) Same as panel (a) but for runs RH2c (solid lines) and RMc (dashed lines). The magnitudes are normalized to the standard deviation of the current. The HMHD runs have wider wings to the distributions than the MHD runs.

structures move or new current structures form. Based on the simulations presented here, times slightly after the peak of Ω_T appear to have more strong current structures providing better statistics in the conditional PDFs. Conditional PDFs have been examined at additional times for both types of initial conditions (see Figs. 8(a) and 8(b) for an example] and while the PDFs for most of the alignments change shape with time, peaks at strong alignment consistently occur for σ_{jb}. Examination of conditional PDFs in the MHD runs (not shown), reveals that, while there may be some association between strong currents and highly aligned σ_{jb}, the association tends to be stronger in HMHD. Evidence has also been found that the inclusion of the Hall term can generate magnetic field-aligned currents in laminar reconnection [79,80].

Figure 9 shows PDFs of the parallel and perpendicular magnitudes of the current with respect to the magnetic field ($|j_\parallel| = |\mathbf{j} \cdot \mathbf{b}|/|\mathbf{b}|$ and $|j_\perp| = \sqrt{|\mathbf{j}|^2 - |j_\parallel|^2}$) for runs OTH2b, OTMb, RH2c, and RMc. Both $|j_\parallel|$ and $|j_\perp|$ have similar PDFs, particularly for the random initial conditions. Even though on average Ω_T is weaker in HMHD, the PDFs extend to greater magnitudes in the case of HMHD consistent with more intermittent behavior. The value of $|j_\parallel|$ reaches nearly the magnitude of the maximum current consistent with the findings of Fig. 7. Stawarz *et al.* [11] have suggested that the destabilization of field-aligned currents plays a key role in the dissipation of collisionless plasma turbulence, particularly in the Earth's magnetotail. The association of intense currents with σ_{jb} and enhancement in current magnitudes in
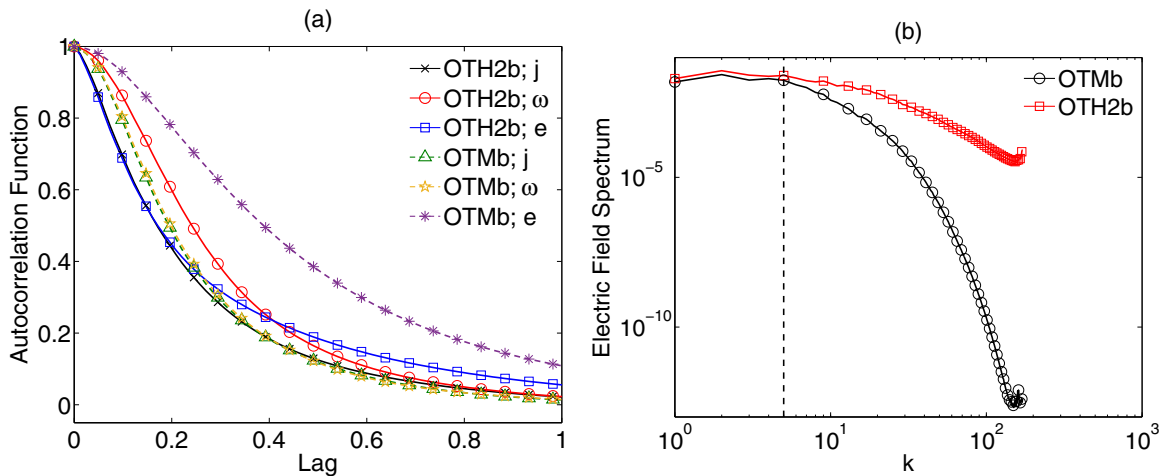

FIG. 10. (Color online) (a) Autocorrelation functions of the current, vorticity, and electric field for runs OTH2b (solid lines) and OTMb (dashed lines). In MHD, the current and vorticity autocorrelation functions are nearly identical consistent with current and vorticity structures that are of similar scales. In HMHD, the current autocorrelation function is narrower and the vorticity autocorrelation function is wider, consistent with thinner current structures and wider vorticity structures. Electric field structures are much narrower and follow the current autocorrelation function at small separations in HMHD. (b) Spectra of $\mathbf{e}$ (Fourier transform of $\mathbf{e}$ autocorrelation function) for runs OTMB (black circles) and OTH2b (red squares). The vertical dashed line marks $1/\epsilon_H$.

HMHD may mean that Hall physics helps to enhance this dissipation mechanism in collisionless plasmas.

From Fig. 7 it appears that the currents are not only significantly more intense than the vorticity in HMHD but also significantly thinner. One way of quantifying the size of structures on average in a turbulent system is by considering the autocorrelation function. Figure 10(a) plots the autocorrelation functions for **j**, ω, and **e** for runs OTH2b and OTMb. The autocorrelation functions are normalized by the mean-square value of each quantity such that the value at zero separation is unity. While in MHD **j** and ω have virtually identical autocorrelation functions consistent with structures of similar size, HMHD has a narrower **j** autocorrelation function and wider ω autocorrelation function. At larger separations the HMHD **j** autocorrelation crosses both the MHD autocorrelation functions indicative of more peaked current structures in HMHD. For MHD the correlation length defined as the integral of the autocorrelation function is 0.042 for both **j** and ω. For HMHD, the correlation lengths are 0.04 for **j** and 0.049 for ω (compared to the total box size of 2π). The behavior of **j** and ω autocorrelation functions is likely a

manifestation of the effect described in Sec. III A which causes ω to scale identically to **b** in the small scales. If $\omega \sim$ **b**, then **j**, which is the curl of **b** will end up being at smaller scale (unless the field is force free).

The HMHD autocorrelation function for the electric field **e** is nearly identical to that of **j** at small separations and then departs from **j**, ultimately becoming wider with a correlation length of 0.048. The presence of **j** structures narrower than **e** structures is consistent with the findings of Bhattacharjee *et al.* [81] in 2D HMHD laminar reconnection. The MHD **e** autocorrelation function is significantly wider than HMHD with a correlation length of 0.081. At small separations the MHD **e** autocorrelation is not identical to **j**. Enhanced small-scale **e** activity has also been observed in 3D HMHD turbulence simulations by Dmitruk and Matthaeus [52]. Smaller-scale **e** activity in HMHD is expected because the Hall term, present in Eq. (4), is important at small scales.

The **e** spectra, which are the Fourier transform of the autocorrelation function, are also shown in Fig. 10(b). At wave numbers below $1/\epsilon_H$ the HMHD and MHD electric field spectra are similar and at wave numbers above $1/\epsilon_H$ HMHD
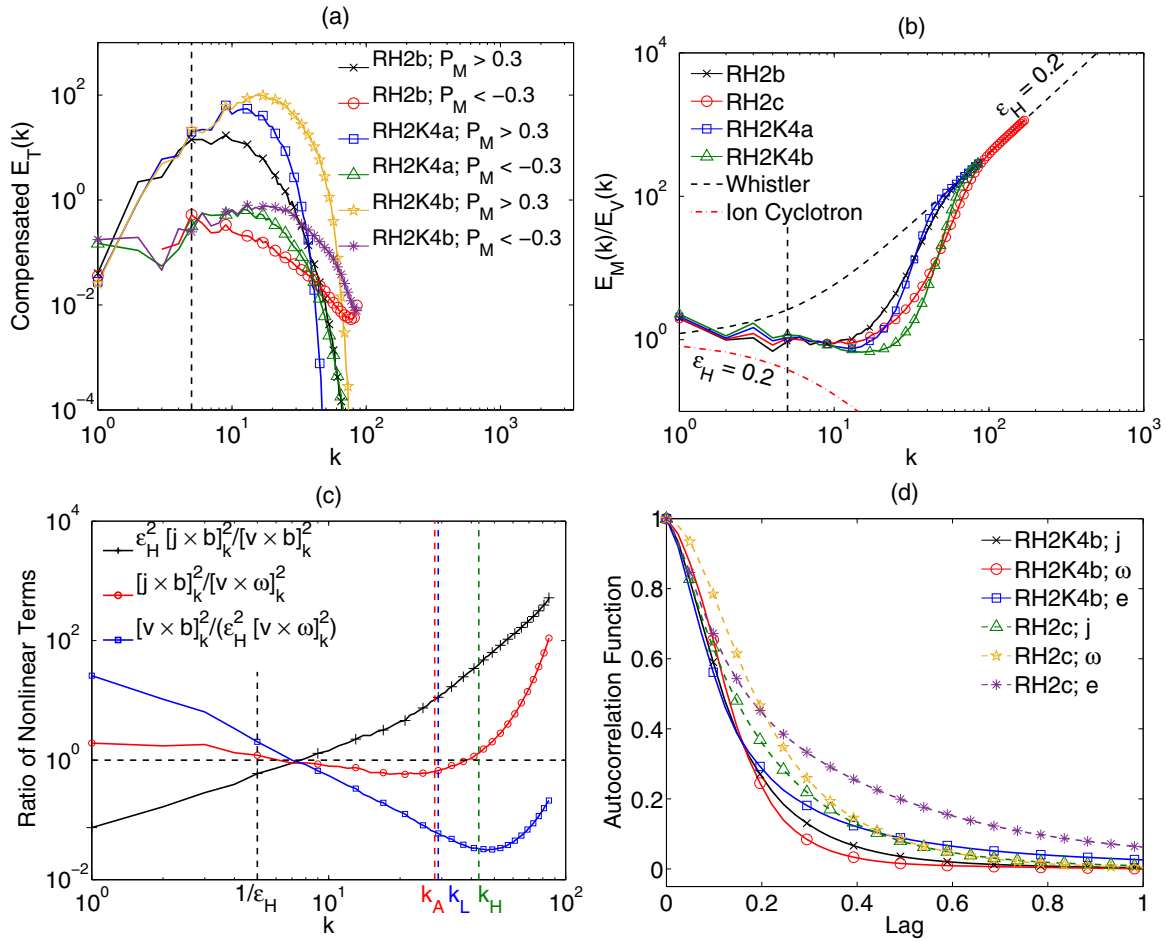

FIG. 11. (Color online) (a) Energy spectra for Fourier modes with $|P_M| > 0.3$ for the two hyperdiffusive runs, as well as run RH2b for comparison. The spectra for negative P_M are compensated by $k^{7/3}$ and the positive P_M spectra are compensated by $k^{11/3}$. The vertical dashed line marks $1/\epsilon_H$. (b) $E_M(k)/E_V(k)$ for the two hyperdiffusive runs with runs RH2b and RH2c (note that this run has 512^3 resolution) for comparison. The vertical dashed line marks $1/\epsilon_H$. (c) Ratio of nonlinear terms in the magnetic vector potential equation, momentum equation, and "uncurled" Ω_L equation for run RH2K4b. The horizontal dashed line denotes unity and the four vertical dashed lines mark the wave numbers $1/\epsilon_H$, k_A, k_L, and k_H. (d) Autocorrelation functions for the current, vorticity, and electric field in run RH2K4b and RH2c for comparison.

has significantly enhanced electric field activity over MHD. The behavior of the electric field spectra are consistent with that reported by Dmitruk and Matthaeus [52].

C. Comparison to hyperdiffusive runs

As has been pointed out by numerous authors [32,41,47], the time scale associated with the Hall term dimensionally scales as k^{-2}, which is the same as the scaling for the diffusive time scale associated with Laplacian dissipation. As such, it has been suggested that from a numerical perspective utilizing hyperdiffusivity may produce better results in that it will allow dissipation to cut in more sharply in the small scales resulting in a better developed HMHD inertial range. The results may then be more comparable to the subion scale nonlinear dynamics present in collisionless plasmas, while still providing sufficient dissipation for the numerics. In order to test if the method of dissipation (regular Laplacian dissipation or hyperdiffusive Laplacian-squared dissipation) alters the results of the previous sections, two hyperdiffusive HMHD runs (see Table I for parameters) are performed and compared to the runs using regular diffusivity. The hyperdiffusive runs are analyzed at the time of maximum of $\mathcal{P}_T$.

In general, runs using hyperdiffusivity give comparable results to the regular diffusivity runs. Some examples are shown in Fig. 11. In Fig. 11(a) the energy spectra for Fourier modes with $|P_M| > 0.3$ are given. While 512^3 resolution regular diffusivity runs seen in Fig. 3 show only short regions that may be consistent with $k^{-7/3}$ scaling for $P_M < -0.3$, the hyperdiffusive runs show regions consistent with $k^{-7/3}$ scaling from just above $1/\epsilon_H$ until $k \sim 30$ in the case of run RH2K4b. However, $P_M > 0.3$ still does not show a significant range of $k^{-11/3}$ scaling. Figure 11(b) shows $E_M(k)/E_V(k)$ for both the hyperdiffusive runs with regular diffusivity runs RH2b and RH2c for comparison. In all runs a transition occurs at scales much shorter than the ion inertial length to a magnetically dominated state following the prediction of Eq. (20) and the wave number of the transition moves to larger values as the diffusivity coefficients are decreased. In the hyperdiffusive runs the transition from near equipartition to $E_M(k)/E_V(k) = \epsilon_H^2 k^2$ is steeper than in the regular viscosity runs. When examining the ratios of the nonlinear terms in the magnetic vector potential (equivalent to the electric field equation), momentum, and "uncurled" $\boldsymbol{\Omega}_T$ equations for run RH2K4b [Fig 11(c)] similar features are seen to the the regular diffusivity run shown in Fig. 6(a). The Hall term dominates the electric field at wave numbers above $k \sim 8$. At $k_A \sim 28$ a transition occurs in the momentum equation where the Lorentz force becomes increasingly important and eventually dominates the equation. The wave number k_A also roughly coincides with the beginning of the transition to the magnetically dominated state in Fig. 11(b) as also found in the regular diffusivity runs. Figure 11(d) shows the autocorrelation functions of $\mathbf{j}$, $\boldsymbol{\omega}$, and $\mathbf{e}$ for runs RH2K4b and RH2c (also see Fig. 10 for another regular diffusivity example). Again the curves show similar general features between hyperdiffusive and regular diffusive runs. At small separations the $\boldsymbol{\omega}$ autocorrelation tends to be wider than the $\mathbf{j}$ autocorrelation with a crossover that occurs at larger separations. The $\mathbf{e}$ autocorrelation is similar to the $\mathbf{j}$ autocorrelation at small separations but ultimately wider at

large separations. Other results discussed in this paper, but not shown in Fig. 11, are likewise similar between hyperdiffusive and regular diffusivity runs.

IV. DISCUSSION AND CONCLUSIONS

In this study, 3D direct numerical simulations of Hall MHD turbulence are examined in both Fourier and real space and compared to MHD simulations. Runs using both traditional Laplacian dissipation and hyperdiffussive Laplacian-squared dissipation are performed and similar results are obtained regardless of the dissipation operator used. It is found that at small to moderate wave numbers, which can extend to scales below the ion inertial length, $E_M(k)/E_V(k)$ is in near equipartition. Unlike MHD, at large wave numbers the ratio becomes magnetically dominated and scales as $\epsilon_H^2 k^2$ which is consistent with the behavior of linear whistler waves. However, it is shown that this scaling is also consistent with nonlinear fluctuations when the $\mathbf{j} \times \mathbf{b}$ terms (Lorentz force and Hall terms) are dominant in the equations. The transition to the magnetically dominated state, which may be akin to the electron MHD regime where ions are taken to be a dynamically unimportant neutralizing background, is found to occur when the $\mathbf{v} \cdot \nabla \mathbf{v}$ term becomes subdominant to dissipation. Unlike MHD, this length scale potentially differs from the overall dissipation scale of the system. The near equipartition of energy into the Hall regime is strongly linked to the nonlinearity of the system, since the $\mathbf{v} \cdot \nabla \mathbf{v}$ term does not contribute to the linearized system. While the simulations presented here are performed in the presence of viscous and resistive dissipation, the results suggest that examination of the ratio of magnetic to kinetic energy spectra may provide insight into the behavior of dissipation in collisionless plasmas or at least provide an indication of the relative importance of the various nonlinearities in the system.

The spectra of right- and left-polarized fluctuations in HMHD turbulence have also been examined in the manner proposed by Meyrand and Galtier [47]. The ratio of $\langle|\mathbf{u}_R|^2\rangle/\langle|\mathbf{u}_L|^2\rangle$ in the initial conditions seems to have an effect on the relative amplitudes of the right- and left-polarized spectra and therefore affects the exact ratio of $E_M(k)/E_V(k)$ in the near equipartition region. Smaller ratios of $\langle|\mathbf{u}_R|^2\rangle/\langle|\mathbf{u}_L|^2\rangle$ appear to be associated with more kinetic energy. The slope of the right- and left-polarized spectra have short regions that may be consistent with $k^{-7/3}$ and $k^{-11/3}$ respectively when considering moderate to large polarizations ($|P_M| > 0.3$) and regular diffusivity. However, when considering just strongly polarized fluctuations ($|P_M| > 0.7$) left-polarized fluctuations show a much steeper spectrum than $k^{-11/3}$ while right polarization has a significant $k^{-7/3}$ region. When using hyperdiffusivity the region consistent with $k^{-7/3}$ is somewhat enhanced for $P_M < -0.3$.

Current structures in HMHD are found to be narrower and more intense than in MHD, as has been noted by various other authors [46,49,51]. In particular, it is found that while current and vorticity structures have nearly equal sizes on average in MHD, in HMHD current structures become narrower and vorticity structures become broader. Evidence is also found that there may be a relationship between the strong current structures and alignment between the current

and magnetic field. This behavior somewhat differs from the idea of strong currents forming in the boundary between regions of strong alignment, which has been proposed in the context of MHD [78,82]. Alignment between **j** and **b** within strong current structures may be of particular importance in collisionless plasmas where intense field-aligned currents can be unstable.

Electric field autocorrelation functions are found to be significantly narrower in HMHD than in MHD and to behave similar to the current autocorrelation function at small separations. The similar behavior to the current autocorrelation may be of use for *in situ* measurements of space plasmas, since the electric field is often easier to obtain than the current. However, further understanding of how additional kinetic effects alter this behavior is necessary to use this feature in space plasmas.

Additional simulations may provide further insight into some of the results found here. In light of the $E_M(k)/E_V(k)$ findings, studies varying the magnetic Prandtl number such that $\nu \neq \eta$ (in particular $\nu < \eta$) may be interesting in HMHD,

since this can alter the ordering of the various dissipation scales and could produce different behavior. Simulations with an explicitly imposed B_0 could provide more insight into the role of the double curl Beltrami configuration in the small scales. Finally, simulations with smaller-scale initial conditions or forcing, such that more strong current structures are generated and better statistics are obtained, would help to characterize the relationship between current structures and alignments.

[1] S. R. Cranmer, Living Rev. Solar Phys. **6**, 3 (2009).

[2] S. R. Cranmer, M. Asgari-Targhi, M. P. Miralles, J. C. Raymond, L. Strachan, H. Tian, and L. N. Woolsey, Phil. Trans. R. Soc. A **373**, 20140148 (2015).

[3] W. H. Matthaeus, J. W. Bieber, and G. P. Zank, Rev. Geophys. Suppl. **33**, 609 (1995).

[4] C.-Y. Tu and E. Marsch, Space Sci. Rev. **73**, 1 (1995).

[5] R. Bruno and V. Carbone, Living Rev. Solar Phys. **10**, 2 (2013).

[6] J. E. Borovsky, R. C. Elphic, H. O. Funsten, and M. F. Thomsen, J. Plasma Phys. **57**, 1 (1997).

[7] J. E. Borovsky and H. O. Funsten, J. Geophys. Res. **108**, 1284 (2003).

[8] J. M. Weygand, M. G. Kivelson, K. K. Khurana, H. K. Schwarzl, S. M. Thompson, R. L. McPherron, A. Balogh, L. M. Kistler, M. L. Goldstein, J. Borovsky, and D. A. Roberts, J. Geophys. Res. 110, A01205 (2005).

[9] J. Saur, H. Politano, A. Pouquet, and W. H. Matthaeus, Astron. Astrophys. **386**, 699 (2002).

[10] J. Saur, A. Pouquet, and W. H. Matthaeus, Geophys. Res. Lett. **30**, 1260 (2003).

[11] J. E. Stawarz, R. E. Ergun, and K. A. Goodrich, J. Geophys. Res. **120**, 1845 (2015).

[12] E. Falgarone, J. Pety, and J. Hily-Blandt, Astron. Astrophys. **507**, 355 (2009).

[13] D. Falceta-Gonçalves, G. Kowal, E. Falgarone, and A. C.-L. Chian, Nonlin. Proc. Geophys. **21**, 587 (2014).

[14] K. H. Kiyani, K. T. Osman, and S. C. Chapman, Phil. Trans. R. Soc. A **373**, 20140155 (2015).

[15] F. Sahraoui, M. L. Goldstein, P. Robert, and Y. V. Khotyaintsev, Phys. Rev. Lett. **102**, 231102 (2009).

[16] F. Sahraoui, M. L. Goldstein, G. Belmont, P. Canu, and L. Rezeau, Phys. Rev. Lett. **105**, 131101 (2010).

[17] H. Karimabadi, V. Roytershteyn, M. Wan, W. H. Matthaeus, W. Daughton, P. Wu, M. Shay, B. Loring, J. Borovsky, E. Leonardis, S. C. Chapman, and T. K. M. Nakamura, Phys. Plasmas **20**, 012303 (2013).

[18] R. J. Leamon, C. W. Smith, N. F. Ness, and H. K. Wong, J. Geophys. Res. **104**, 22331 (1999).

[19] S. D. Bale, P. J. Kellogg, F. S. Mozer, T. S. Horbury, and H. Reme, Phys. Rev. Lett. **94**, 215002 (2005).

[20] G. G. Howes, J. M. TenBarge, W. Dorland, E. Quataert, A. A. Schekochihin, R. Namata, and T. Tatsuno, Phys. Rev. Lett. **107**, 035004 (2011).

[21] D. Biskamp, E. Schwarz, and J. F. Drake, Phys. Rev. Lett. **76**, 1264 (1996).

[22] S. P. Gary, S. Saito, and Y. Narita, Astrophys. J. **716**, 1332 (2010).

[23] J. C. Kasper, A. J. Lazarus, and S. P. Gary, Phys. Rev. Lett. **101**, 261103 (2008).

[24] O. Alexandrova, C. H. K. Chen, L. Sorriso-Valvo, T. S. Horbury, and S. D. Bale, Space Sci. Rev. **178**, 101 (2013).

[25] R. E. Ergun, L. Andersson, J. Tao, V. Angelopoulos, J. Bonnell, J. P. McFadden, D. E. Larson, S. Eriksson, T. Johansson, C. M. Cully, D. N. Newman, M. V. Goldman, A. Roux, O. LeContel, K.-H. Glassmeier, and W. Baumjohann, Phys. Rev. Lett. **102**, 155002 (2009).

[26] R. E. Ergun, K. A. Goodrich, J. E. Stawarz, L. Andersson, and V. Angelopoulos, J. Geophys. Res. **120**, 1832 (2015).

[27] S. L. G. Hess, D. M. Malaspina, and R. E. Ergun, J. Geophys. Res. 116, A07104 (2011).

[28] K. T. Osman, W. H. Matthaeus, K. H. Kiyani, B. Hnat, and S. C. Chapman, Phys. Rev. Lett. **111**, 201101 (2013).

[29] J. L. Burch, T. E. Moore, R. B. Torbert, and B. L. Giles, Space Sci. Rev. 1 (2015).

[30] D. Biskamp, E. Schwarz, and J. F. Drake, Phys. Plasmas **4**, 1002 (1997).

[31] M. A. Shay and J. F. Drake, Geophys. Rev. Lett. **25**, 3759 (1998).

[32] J. Birn, J. F. Drake, M. A. Shay, B. N. Rogers, R. E. Denton, M. K. M. Hesse, Z. W. Ma, A. Bhattacharjee, A. Otto, and P. L. Pritchett, J. Geophys. Res. **106**, 3715 (2001).

[33] F. S. Mozer, S. D. Bale, and T. D. Phan, Phys. Rev. Lett. **89**, 015002 (2002).

[34] A. L. Borg, M. O. ieroset, T. D. Phan, F. S. Mozer, A. Pedersen, J. P. MacPhadden, C. Twitty, A. Balogh, and H. Rème, Geophys. Res. Lett. **32**, L19105 (2005).

[35] M. Yamada, Y. Ren, H. Ji, J. Breslau, S. Gerhardt, R. Kulsrud, and A. Kuritsyn, Phys. Plasmas **13**, 052119 (2006).

[36] W. H. Matthaeus and M. Goldstein, J. Geophys. Res. **87**, 6011 (1982).

[37] P. D. Mininni and A. Pouquet, Phys. Rev. Lett. **99**, 254502 (2007).

[38] C. H. K. Chen, L. Leung, S. Boldyrev, B. A. Maruca, and S. D. Bale, Geophys. Res. Lett. **41**, 8081 (2014).

[39] C. Liu, X. Feng, J. Guo, and Y. Ye, J. Geophys. Res. **118**, 2087 (2013).

[40] S. Galtier, J. Plasma Phys. **72**, 721 (2006).

[41] S. Ghosh, E. Siregar, D. A. Roberts, and M. A. Goldstein, J. Geophys. Res. **101**, 2493 (1996).

[42] V. Krishan and S. M. Mahajan, Nonlin. Proc. Geophys. **12**, 75 (2005).

[43] O. Alexandrova, V. Carbone, P. Veltri, and L. Sorriso-Valvo, Astrophys. J. **674**, 1153 (2008).

[44] D. Hori and H. Miura, Plasma Fusion Res. **3**, S1053 (2008).

[45] D. Shaikh and P. K. Shukla, Nonlin. Proc. Geophys. **16**, 189 (2009).

[46] H. Miura and D. Hori, J. Plasma Fusion Res. Ser. **8**, 73 (2009).

[47] R. Meyrand and S. Galtier, Phys. Rev. Lett. **109**, 194501 (2012).

[48] W. H. Matthaeus, P. Dmitruk, D. Smith, S. Ghosh, and S. Oughton, Geophys. Rev. Lett. **30**, 4 (2003).

[49] H. Miura and K. Araki, J. Phys.: Conf. Ser. **318**, 072032 (2011).

[50] P. D. Mininni and A. Pouquet, Phys. Rev. E **80**, 025401 (2009).

[51] S. Donato, S. Servidio, P. Dmitruk, M. A. Shay, P. A. Cassak, and W. H. Matthaeus, Phys. Plasmas **19**, 092307 (2012).

[52] P. Dmitruk and W. H. Matthaeus, Phys. Plasmas **13**, 042307 (2006).

[53] P. D. Mininni, A. Alexandros, and A. Pouquet, J. Plasma Phys. **73**, 377 (2007).

[54] L. N. Martin, P. Dmitruk, and D. O. Gomez, Phys. Plasmas **19**, 052305 (2012).

[55] P. R. Imazio, L. N. Martin, P. Dmitruk, and P. D. Mininni, Phys. Plasmas **20**, 052506 (2013).

[56] L. N. Martin, G. DeVita, L. Sorriso-Valvo, P. Dmitruk, G. Nigro, L. Primavera, and V. Carbone, Phys. Rev. E **88**, 063107 (2013).

[57] J. E. Stawarz, A. Pouquet, and M.-E. Brachet, Phys. Rev. E **86**, 036307 (2012).

[58] S. M. Mahajan and Z. Yoshida, Phys. Rev. Lett. **81**, 4863 (1998).

[59] L. Turner, IEEE Trans. Plasma Sci. **14**, 849 (1986).

[60] F. Sahraoui, S. Galtier, and G. Belmont, J. Plasma Phys. **73**, 723 (2007).

[61] P. D. Mininni, D. Rosenberg, R. Reddy, and A. Pouquet, Parallel Comput. **37**, 316 (2011).

[62] D. Biskamp and H. Welter, Phys. Fluids B **1**, 1964 (1989).

[63] H. Politano, A. Pouquet, and P. L. Sulem, Phys. Plasmas **2**, 2931 (1995).

[64] O. Podvigina and A. Pouquet, Physica D **75**, 471 (1994).

[65] S. Galtier and E. Buchlin, Astrophys. J. **656**, 560 (2007).

[66] K. R. Sreenivasan and R. A. Antonia, Ann. Rev. Fluid Mech. **29**, 435 (1997).

[67] D. Porter, A. Pouquet, and P. Woodward, Phys. Rev. E **66**, 026301 (2002).

[68] L. Sorriso-Valvo, V. Carbone, P. Veltri, H. Politano, and A. Pouquet, EuroPhys. Lett. **51**, 520 (2000).

[69] P. D. Mininni, A. G. Pouquet, and D. C. Montgomery, Phys. Rev. Lett. **97**, 244503 (2006).

[70] B. T. Tsurutani and C. M. Ho, Rev. Geophys. **37**, 517 (1999).

[71] W. H. Matthaeus, M. Wan, S. Servidio, A. Greco, K. T. Osman, S. Oughton, and P. Dmitruk, Phil. Trans. R. Soc. A **373**, 20140154 (2015).

[72] P. A. Davidson, *Turbulence: An Introduction for Scientists and Engineers* (Oxford University Press, New York, 2004).

[73] K. T. Osman, W. H. Matthaeus, M. Wan, and A. F. Rappazzo, Phys. Rev. Lett. **108**, 261102 (2012).

[74] M. Wan, W. H. Matthaeus, H. Karimabadi, V. Roytershteyn, M. Shay, P. Wu, W. Daughton, B. Loring, and S. C. Chapman, Phys. Rev. Lett. **109**, 195001 (2012).

[75] J. M. TenBarge and G. G. Howes, Astrophys. J. Lett. **771**, L27 (2013).

[76] E. Lee, M.-E. Brachet, A. Pouquet, P. D. Mininni, and D. Rosenberg, Phys. Rev. E **78**, 066401 (2008).

[77] A. Pouquet, M.-E. Brachet, E. Lee, P. D. Mininni, D. Rosenberg, and V. Uritsky, Proc. Int. Astron. Union **6**, 304 (2010).

[78] M. Meneguzzi, H. Politano, A. Pouquet, and M. Zolver, J. Comp. Phys. **123**, 32 (1996).

[79] Z. W. Ma and L. C. Lee, J. Geophys. Res. **106**, 25951 (2001).

[80] X. Ma and A. Otto, J. Geophys. Res. **118**, 4906 (2013).

[81] A. Bhattacharjee, Z. W. Ma, and X. Wang, Phys. Plasmas **8**, 1829 (2001).

[82] S. Servidio, W. H. Matthaeus, and P. Dmitruk, Phys. Rev. Lett. **100**, 095005 (2008).